

# Single-Pixel Imaging for Partially Occluded Objects

Jingjing Wu , Lifa Hu, and Jicheng Wang 

**Abstract**—In some complex scene, such as military reconnaissance and other fields, the target object may be partially occluded by some opaque obstacles, which increase the difficulty to obtain the complete object image. In traditional optical imaging system, the lenslet array or the reference beam and special algorithms are usually needed to solve this problem, which increase the complexity of the system. As a computational optical imaging technology, the problem of single-pixel imaging (SPI) for an occluded object has not been researched yet as we know. Here we propose an SPI system to recover the occluded object image. Firstly, the images of object and occlusion from different perspectives are obtained by detecting the light field at different positions. Secondly, the limited conditions of the system parameters are derived by using geometric optics theory to ensure complete imaging. Thirdly, the feasibility of the scheme and the correctness of the limited conditions are verified by experiments. The results in this article can promote the application of SPI technology in many complex practices.

**Index Terms**—Image reconstruction techniques, occluded object imaging, single-pixel imaging.

## I. INTRODUCTION

COMPUTATIONAL optical imaging (COI) technology has developed rapidly in recent years and has achieved significant results in various fields, including super-resolution imaging [1], single-photon imaging [2], and non-line-of-sight imaging [3]. Single-pixel imaging (SPI) is one of the COI technologies, in which the object is projected onto a digital mirror device (DMD) and modulated by the patterns loaded in the DMD. The intensity of reflected light from the DMD is detected by a single-pixel detector such as a photoelectric detector (PD). After repeating the modulate and detect process, the patterns and detected intensities are calculated to recover the 2D image of the object [4].

Because of the special imaging mechanism, SPI has been used in terahertz imaging [5], X-ray imaging [6], [7], 3D imaging [8], [9], and imaging in the complicated environments [10], [11], [12], [13]. Therein, SPI has high robustness in the complicated environments and can be used to image the object through scattering medium, such as biological samples and atmosphere turbulence.

In some complicated scenes, the target object is occluded by an opaque obstacle, part of the information would be lost and the recovered object image would be incomplete. If the diffraction

effect is strong, the occluded object information can diffract the obstacle and be detected by the PD and then recovered by special algorithms. The diffraction effect is affected by the wavelength, the size of the object, and the obstacle. In 2016, the influence of black netting material on the 3D-SPI was analyzed [14]. In 2019, Gao et al. analyzed the effect of the distance between the object and occlusion and the wavelength on the imaging quality of SPI [15]. On the contrary, if the diffraction effect is weak, the information in the occluded area cannot diffract the obstacle and reach the PD, therefore it cannot be recovered by algorithms. To our knowledge, the SPI method aiming at this situation are not researched until now.

In traditional optical imaging systems, one of the effective methods to realize the partially occluded object reconstruction is computational integral imaging, especially for occluded 3D objects [16], [17], [18], [19], [20]. This method commonly uses a microlens array and a recording sensor to record the elemental images. Then the recorded elemental images are digitally reconstructed by using some special algorithms [20]. An alternative method is compressive Fresnel holography [21], in which the light field of the object is partially occluded by the obstacle and then interferes with a reference wave on the detector. The object is recovered from the digitally recorded hologram using compressive sensing. For these two methods above, the lenslet array or the reference beam and special algorithms are needed, which increase the complexity of the system.

In this article, SPI system for the partially occluded object is analyzed. Different from previous works, we consider the weak diffraction situation. In the proposed SPI system, the modulated object information is detected by the PD through an optical fiber. By changing the position of the fiber probe, the different perspective images of the object and obstacle can be recovered. For each perspective image, the obstacle area is removed and the object area is retained by using the region growing method. If the positions of the fiber probe satisfy the condition, the complete object image can be obtained by adding all the perspective images. The detailed condition is derived from geometrical optics theory. The experiments for different objects and obstacles are performed and prove the feasibility of the proposed method.

## II. PROPOSED METHOD

The conventional optical system diagram of SPI is shown in Fig. 1(a). The object is illuminated and the reflected light is projected on the DMD and modulated. Then the reflected light from the DMD is detected by a PD. After a series of modulation and detection, the object image can be recovered by optimization algorithms according to compressive sensing.

Manuscript received 30 April 2023; revised 19 May 2023; accepted 29 May 2023. Date of publication 1 June 2023; date of current version 14 June 2023. This work was supported by the National Natural Science Foundation of China under Grant 62205127. (Corresponding author: Jingjing Wu.)

The authors are with the School of Science, Jiangnan University, Wuxi 214122, China (e-mail: ftxbs123@163.com; hulifa@jiangnan.edu.cn; jcwang@jiangnan.edu.cn).

Digital Object Identifier 10.1109/JPHOT.2023.3281820

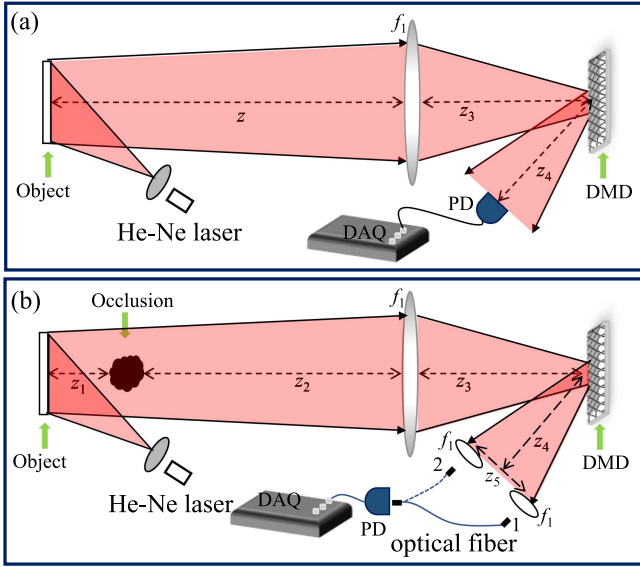


Fig. 1. Setup of SPI for the object (a) without obstacle and (b) with an obstacle.

### A. Description of the Proposed SPI System

When an obstacle is put between the object and projection lens, the recovered SPI image of a signal PD would contain the information of the object and the obstacle at the same time. When the diffraction effect is negligible, the recovered image can be represented as

$$I(x, y) = O(x, y) \times M^O(x, y) + T(x, y) \times M^T(x, y) \quad (1)$$

in which  $O(x, y)$  represents the object image.  $T(x, y)$  represents the obstacle.  $M^O(x, y)$  and  $M^T(x, y)$  represent the object area and the occluded area, respectively. The information of object in the occluded area cannot arrive at the PD, therefore, the object image is incomplete. In our work, an optical fiber is used, which is shown in Fig. 1(b). When the information of the object and the obstacle is projected on the DMD, the object is in focus, and the obstacle is out of focus. The reflected light from the DMD is detected by the PD through an optical fiber. The SPI image can be obtained through the detected signals of PD. If the position of the optical fiber is changed from 1 to 2, which is shown as Fig. 1(b), the position of the object in the SPI result is still fixed, while the position of the obstacle is changed. According to Ref. [22], the corresponding displacement of the obstacle is related to  $z_1$ ,  $z_4$ , and  $z_5$ , where  $z_1$  represents the distance between the object and obstacle,  $z_4$  represents the distance between the DMD and probe, and  $z_5$  represents the displacement of the fiber from 1 to 2. Suppose the recovered images in the two positions are  $I_1(x, y)$  and  $I_2(x, y)$ , respectively. In  $I_1(x, y)$  and  $I_2(x, y)$ ,  $M_1^O(x, y)$  and  $M_1^T(x, y)$ ,  $M_2^O(x, y)$  and  $M_2^T(x, y)$ , are changed with the perspective of the image. If  $z_5$  is large enough, the complete object information would be contained in the recovered images.

After obtaining the SPI images  $I_1(x, y)$  and  $I_2(x, y)$ , the obstacle areas should be picked and removed from them. If the obstacle areas in  $I_1$  and  $I_2$  can be picked and removed, the complete object image can be recovered. The flowchart of the proposed

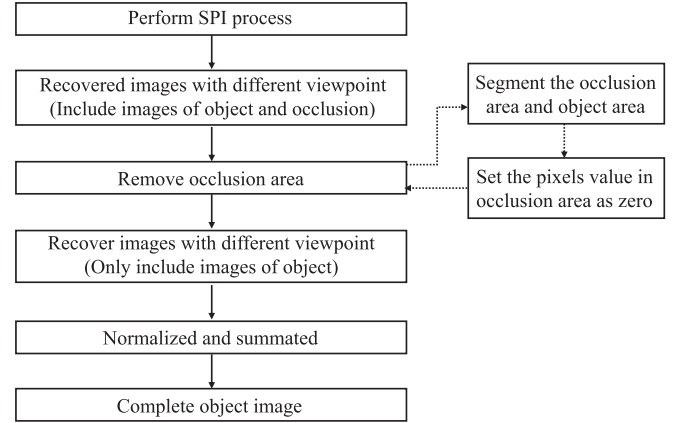


Fig. 2. Flowchart of image processing in the proposed system.

SPI scheme for the occluded object is shown in Fig. 2, and the detailed processes are described as below:

*Step 1:* Perform the SPI process when the optical fiber is in position 1 and 2 successively.

*Step 2:* The TVAL3 algorithm [23], [24], one of the most commonly used compressive sensing reconstruction algorithms, is used to calculate the two perspective images  $I_1$  and  $I_2$ . The use of the TVAL3 algorithm can decrease the needed sampling number of SPI and increase the imaging speed. In the recovered images, the object is partly occluded by the obstacle.

*Step 3:* Pick out and remove the obstacle area. For each SPI image, the obstacle area is designated and the image is divided into object area and obstacle area.

The stereo matching algorithm is a popular approach for occlusion segmentation and object identification in stereo vision technology. While the accuracy of the algorithm largely relies on the resolution, color, structure and other minute details of the perspective images. If the sampling number and the image quality of SPI are high, the stereo-matching algorithms can be used. While for SPI, the image quality is not as high as the camera result when the sampling number is low. Therefore, the segmentation of occlusion is more difficult.

In this article, we consider that the object structure is simple, and the reflection of the obstruction is near the object, i.e., pixel values of the obstruction region are closer to pixel values of objects in SPI image results. To identify the obstacle area, firstly, identify a small area as the obstacle region. Secondly, select one point from that region as the seed point. Finally, utilize the region growing method to pinpoint the exact area of the obstacle.

The detailed processes of seed point selection and region segmentation are as follows:

- 1) Image preprocessing. Specifically, the two SPI images are denoised using Gaussian filtering and then separately binarized into binary images  $BI_1$  and  $BI_2$ .

$$DI_1 = \begin{cases} 1, & \text{if } BI_1 = 1 \text{ and } BI_2 = 0; \\ 0, & \text{else.} \end{cases} \quad (2)$$

- 
1. Input: Image  $I$ , seed point  $(x, y)$ , growth threshold;
  2. Output: Label mask  $M$ ;
  3. Initialization: Set seed point gray value  $\text{seed} = I(x, y)$ ;  
Label image  $M$  is all zeros,  $M(x, y) = 1$ ;  $\text{area\_sum} = \text{seed}$ ;  $\text{area\_count} = 1$ ;
  4. Iterative region growing:  
while  $\text{area\_count} > 0$   
  new marked points  $\text{area\_count} = 0$   
  Traverse each pixel  $(i, j)$  of the image  $I$ :  
  if  $M(i, j) = 1$   
    forall pixel points  $(i + u, j + v)$ ,  $u, v \in \{-10, 1\}$  in the neighborhood:  
    if  $M(i+u, j+v) = 0$  &  $|I(i+u, j+v) - \text{seed}| < = \text{threshold}$   
      Mark the point:  $M(i + u, j + v) = 1$   
       $\text{area\_count} = \text{area\_count} + 1$   
       $\text{area\_sum} = \text{area\_sum} + I(i + u, j + v)$   
    end forall  
   $\text{seed} = \text{area\_sum} / \text{area\_count}$   
end while
  5. End, output label mask  $M$ .
- 

$$DI_2 = \begin{cases} 1, & \text{if } BI_1 = 0 \text{ and } BI_2 = 1; \\ 0, & \text{else.} \end{cases} \quad (3)$$

Due to the low quality of SPI images, slight differences may exist between  $DI_1$  and  $DI_2$  even if there is no obstruction. Consequently, in addition to obstacle regions, small spurious regions would also present in  $DI_1$  and  $DI_2$ . To eliminate these spurious regions, morphological erosion is applied, and the largest remaining region is selected as the labeled obstacle areas,  $DI_1$  and  $DI_2$ .

- 2) Seed points are selected for region growing. Two random points in the  $DI_1$  and  $DI_2$  are chosen as the seed points, respectively.
- 3) The region growing method is utilized with the selected seed points to perform image segmentation and obtain obstacle area masks  $M_1$  and  $M_2$ . After selecting  $DI_1$  and  $DI_2$  as the seed points of images  $I_1$  and  $I_2$  respectively, the region growing method is used to obtain masks  $M_1$  and  $M_2$ . The region growing method usually segments areas by comparing the seed points with the gray value, texture, color and other information of the areas. The judgment rule adopted in this article is the gray value. To describe the process clearly, the process of the specific method is given as follows:

To eliminate the boundary effect of the masks, morphological dilation is applied.

*Step 4:* The complete images can be recovered by

$$O_1 = I_1 \times (1 - M_1) + I_2 \times M_1 \quad (4)$$

$$O_2 = I_2 \times (1 - M_2) + I_1 \times M_2 \quad (5)$$

$$O = O_1 + O_2 \quad (6)$$

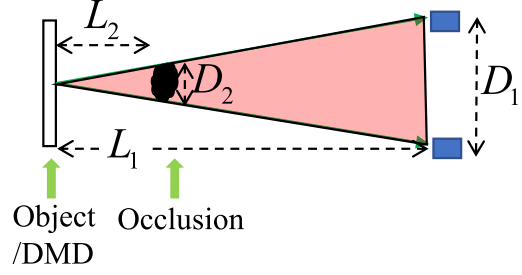


Fig. 3. Equivalent system of Fig. 1(b).

### B. Limitation Analysis of the Displacement of the Optical Fiber Probe

If the displacement of the optical fiber is large enough, the complete object information would be contained in the recovered images. In this part, the limitation of the displacement is analyzed.

The system in Fig. 1(b) is equivalent to Fig. 3 according to Ref. [22]. Based on the principles of geometrical optics, in order to recover the complete image, the displacement  $D_1$  of the fiber probes should be larger than a limiting value. At the limiting value of  $D_1$ , the emitted light from a specific point on the object is exactly unobstructed by the obstacle, which is illustrated in Fig. 3.  $L_1$  represents the distance between the DMD and the fiber probe, which is corresponding to the value  $z_4$  in Fig. 1(b).  $L_2$  represents the distance between the images of the object and the obstacle after the lens imaging. Because the object and the obstacle are both imaged by the lens with the focal length  $f$ , it can be calculated that  $L_2 = \frac{z_2 f}{z_2 - f} - z_3$ .  $D_2$  represents the lateral size of the obstacle after the lens imaging. According to the ratio,  $D_2 = \frac{D_0 f}{z_2 - f}$ , in which  $D_0$  is the actual lateral size of the obstacle. Therefore, the limiting value of  $D_1$  can be calculated by

$$D_1 = \frac{D_2 L_1}{L_2} = \frac{D_0 f z_4}{z_2 f - z_3(z_2 - f)} \quad (7)$$

The value of  $D_1$  in (7) represents the minimum displacement of the fiber probe to recover the complete object image.

## III. EXPERIMENT RESULTS AND ANALYSIS

### A. Feasibility Testing Experiment

The first experiment is used to verify that the perspective of the image is changing with the position of fiber probe. The object is the number “3”, and the obstacle is a black paperboard, which are shown in Fig. 4(a)–(b). The experiment system is shown in Fig. 1(b). The object is illuminated by a He-Ne laser with a wavelength of 632.8 nm. The obstacle is not illuminated. The size of the object and the obstacle and other system parameters are shown in Table I. The modulation patterns are random 0/1 patterns with a ratio of 1:1. The pixel size of the illumination pattern used is  $128 \times 128$  pixels. When loading the illumination pattern onto the DMD,  $8 \times 8$  pixels on the DMD are used as one pixel unit, that is,  $1024 \times 1024$  pixels on the DMD are

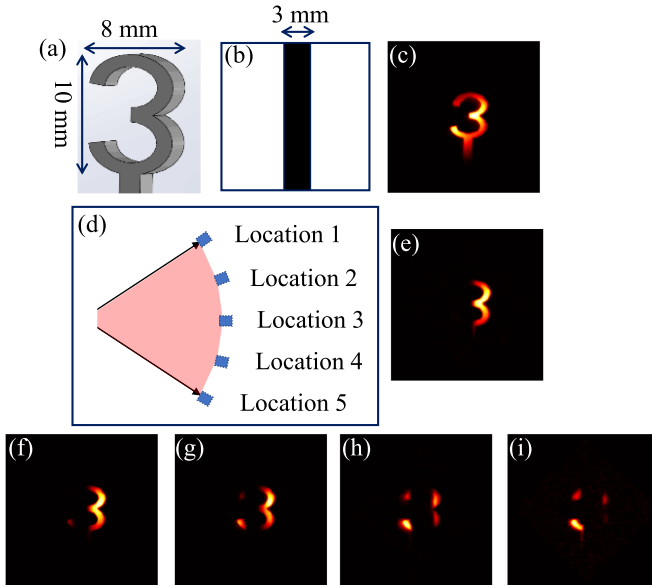


Fig. 4. Feasibility test experiment. (a) Object. (b) Obstacle. (c) SPI result without obstacle. (d) Different positions of fiber probe. (e)–(i) Corresponding SPI results when fiber probe is put in locations 1-5.

TABLE I  
EXPERIMENT PARAMETERS FOR “3” OBJECT. UNITS: MM

Object size	Width of obstacle	$z_1$	$z_2$	$z_3$	$z_4$	$z_5$
10×8	3.0	30.0	320.0	140.0	195.0	10.0

utilized to load the  $128 \times 128$  pixels illumination pattern. The sampling number is  $N = 4000$ . Fig. 4(c) shows the SPI result when the object is not occluded. When the obstacle is existing and the fiber probe is put in locations 1-5 successively as shown in Fig. 4(d), the corresponding recovered SPI images are shown in Fig. 4(e)–(i).

Because the obstacle is not illuminated, only the profile of the obstacle is visible in the SPI results. We can see that the occluded area of the object is moving with the location of the fiber probe. This experiment results prove the feasibility of the proposed method. Next, we will test the situation that the object and the obstacle are both illuminated.

### B. Experiment for “3” Object

In the second experiment, the experiment system is shown as Fig. 1(b). The light source is still the He-Ne laser with a wavelength of 632.8 nm. The modulation patterns loaded on the DMD are random 0/1 patterns with a ratio of 1:1. The detailed system parameters are shown in Table II. The sampling number is 4000.

According to the experiment parameters in Table I and (7), we can calculate that the limiting minimum interval of the fiber probe is 32.5 mm. In our experiment, the interval is  $z_5 = 40.0$  mm, which is larger than the minimum value. Therefore, in theory, the complete image can be recovered.

TABLE II  
EXPERIMENT PARAMETERS OF “3” OBJECT. UNITS: MM

Object size	Width of obstacle	$z_1$	$z_2$	$z_3$	$z_4$	$z_5$
19×10	2.0	30.0	320.0	140.0	195.0	40.0

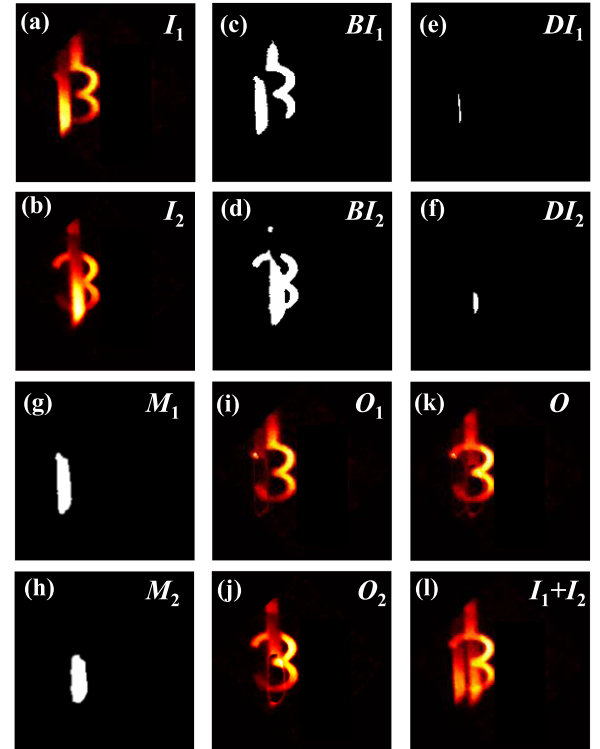


Fig. 5. Experiment results for “3” with the obstacle. (a)–(b) SPI results  $I_1$  and  $I_2$ . (c)–(d) Binarized results  $BI_1$  and  $BI_2$ . (e)–(f) Labeled obstacle areas,  $DI_1$  and  $DI_2$ . (g)–(h) The picked obstacle areas  $M_1$  and  $M_2$  by using the proposed method. (i)–(k) Recovered results of  $O_1$ ,  $O_2$ , and  $O$  by using the proposed method according to (4)–(6). (l)  $I_1+I_2$ .

Fig. 5(a)–(b) show the two recovered SPI images  $I_1$  and  $I_2$  when the fiber probe is put in position 1 and 2, which is shown in Fig. 1(b). Fig. 5(a)–(b) show that the pixel value of the obstacle and the object are very similar to each other, which increase the difficulty to separate the obstacle and the object. Also, we can see that the position of the object is stable in  $I_1$  and  $I_2$ , while the occluded area is changed with the position of fiber probe. Fig. 5(c)–(d) show the binarized images  $BI_1$  and  $BI_2$  of  $I_1$  and  $I_2$ . Fig. 5(e)–(f) show the labeled obstacle areas,  $DI_1$  and  $DI_2$ , respectively. Fig. 5(g)–(h) show the picked obstacle areas by using the proposed method,  $M_1$  and  $M_2$ , which are obtained through the region growing method. Fig. 5(i)–(k) show the image  $O_1$ ,  $O_2$ , and  $O$ , respectively. For comparison, Fig. 5(l) shows the image of  $I_1+I_2$ . Comparing Fig. 5(i)–(k) with Fig. 5(l) we can see that the proposed method can remove the obstacle effectively and can obtain the complete object image. Even though the chosen obstacle area in Fig. 5(g)–(h) is not identical to the actual

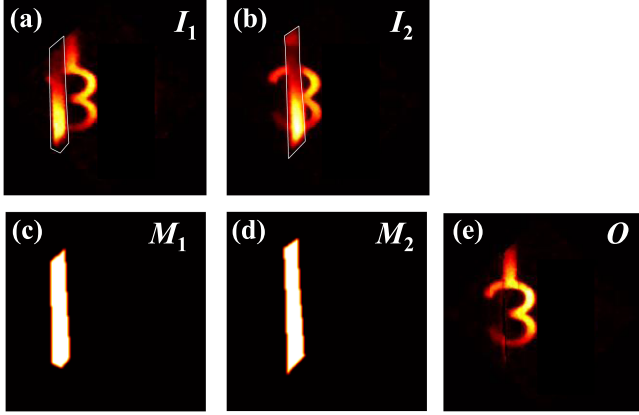


Fig. 6. Results for artificially picked method. (a)–(b) Artificially picked area in  $I_1$  and  $I_2$ . (c)–(d) Artificially picked  $M_1$  and  $M_2$ . (e) Recovered image.

TABLE III  
EXPERIMENT PARAMETERS OF THE “HOUSE” OBJECT. UNITS: MM

Object size	Effective width of obstacle	$z_1$	$z_2$	$z_3$	$z_4$	$z_5$
21×20	3.53	40.0	395.0	130.0	195.0	80.0

TABLE IV  
EXPERIMENT PARAMETERS OF THE “CAR” OBJECT. UNITS: MM

Object size	Effective width of obstacle	$z_1$	$z_2$	$z_3$	$z_4$	$z_5$
20×20	2.0~6.0	40.0	395.0	130.0	195.0	80.0

obstacle area, the object information in the recovered image is complete and unambiguous.

If the obstacle areas in  $I_1$  and  $I_2$  are picked artificially, the picked results and the recovered image are shown in Fig. 6. In the artificially picked method, the obstacle areas are first recognized by visually comparing two input images. Several pixel points surrounding the obstacle areas are then manually signed. Finally, the contour formed by the signed pixel points is designated as the boundary of the obstacle. Clearly, the artificially picked method has a high accuracy. Therefore, its outputs are benchmarked against the results of the proposed method, thereby demonstrating the effectiveness of our approach. The correlation coefficients values (CC) between Figs. 6(e) and 5(i)–(k) are 0.9556, 0.9144, and 0.9758, which prove the reliability of the proposed method.

### C. Experiment for the “House” Object

In the third experiment, a gray object is used instead of the binary object above. The light source and the modulation patterns are the same with Section III-B. The size of the object and obstacle, as well as the system parameters, are summarized in Table III.

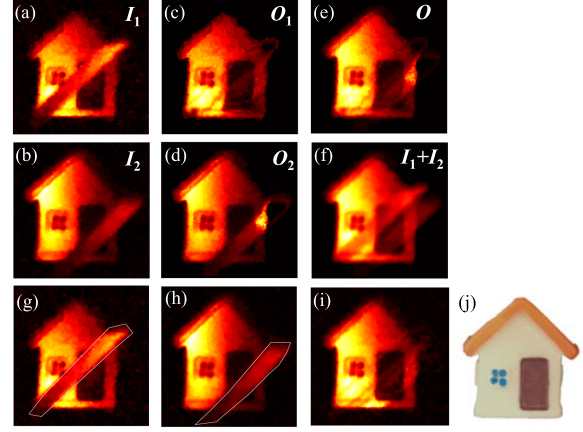


Fig. 7. Experiment results for the “House” with the obstacle. (a)–(b) SPI results  $I_1$  and  $I_2$ . (c)–(e) Recovered results of  $O_1$ ,  $O_2$ , and  $O$  by using the proposed method according to (4)–(6). (f)  $I_1+I_2$ . (g)–(i) Results for artificially picked occluded areas. (j) Object model.

The width of the actual obstacle is 2.5 mm. Because the obstacle is slant and the angle is about 45 degrees, therefore the equivalent width of the occlusion is about 3.53 mm. According to (7), the minimum interval of the fiber probe is about 60.0 mm. In our experiment, the interval is  $z_5 = 80.0$  mm, which is larger than the minimum value. The sampling number is still 4000.

Fig. 7(a)–(b) show the two recovered SPI images  $I_1$  and  $I_2$ , and Fig. 7(j) shows the actual object. From Fig. 7(a)–(b) we can see that the dark color area (the door and the window) in the object appears to be black and the pixel values are approaching background noise because of the low sampling number. We also can see that the intensity of the obstacle is similar to that of the object.

Fig. 7(c)–(e) show the results of  $O_1$ ,  $O_2$ , and  $O$ , respectively. For comparison, Fig. 7(f) shows the image of  $I_1+I_2$ .

Comparing Fig. 7(c)–(e) with Fig. 7(f) we can see that the proposed method can remove the obstacle effectively and can obtain the complete object image. If the obstacle areas in  $I_1$  and  $I_2$  are picked artificially, the picked results and the recovered image are shown in Fig. 7(g)–(i). The CC values between Fig. 7(i) and 7(c)–(e) are 0.9597, 0.9197, and 0.9675, respectively.

### D. Experiment for the “Car” Object

The parameters of the system used in the fourth experiment are identical to those in Fig. 7 except the sizes of the object and obstacle are different, which are shown in Table IV. Specifically, the obstacle is an oblique curved object that has an effective width between 2.0 and 6.0 mm. According to (2) and taking into consideration the slant of the obstacle, the minimum interval of the fiber probe is about 33.9 mm for 2.0 mm obstacle and 101.7 mm for 6.0 mm obstacle. In this experiment, the interval is 80 mm, hence the recovered occluded areas from the two SPI images are overlapping with each other. Therefore, the obstacle cannot be removed completely, which is shown in Fig. 8(c)–(e). This result is in accord with the artificial result in Fig. 8(i). The CC values between Fig. 8(i) and (c)–(e) are 0.8588, 0.8936, and 0.9460, respectively.

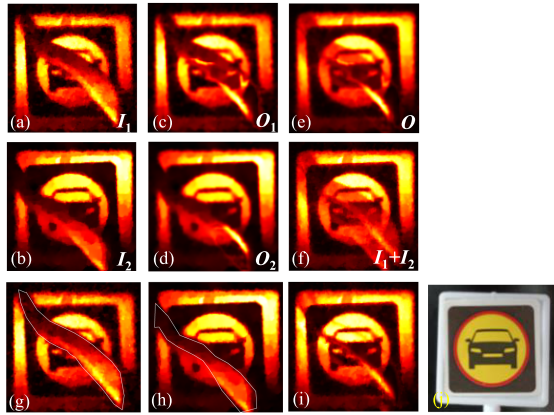


Fig. 8. Experiment results for the “Car” with the obstacle. (a)–(b) SPI results  $I_1$  and  $I_2$ . (c)–(e) Recovered results of  $O_1$ ,  $O_2$ , and  $O$  by using the proposed method according to (4)–(6). (f)  $I_1+I_2$ . (g)–(i) Results for artificially picked occluded areas. (j) Object image.

#### IV. CONCLUSION

It is a challenge to image an occluded object by using single-pixel imaging (SPI), which has not been researched deeply yet as we know. This study focuses on this practical optical imaging issue and provides the imaging system, the data processing method, the theoretical analysis of the experiment parameters, and the experiment results. The proposed system is aiming at a situation where the diffraction effect is negligible, which is different from the existing works. Because of the low image quality of SPI, occlusion removal is more difficult than in a camera-based imaging system. The results using the proposed occlusion pick and remove method are comparable with that of the artificial method. We believe that the proposed SPI system can be used in many practical application situations, especially in complicated scenes.

In this article, the optical fiber probe is moved to obtain the two perspective images. As an alternative method, a camera is also can be used instead of the combination of PD and optical fiber. The different areas in the camera can be treated as many PDs in different positions. While the acquisition rate of camera is relatively lower than PD, and the subsequent image processing algorithm is needed to extract the information from the detected images of camera. Therefore, the combination of PD and optical fiber is used in the proposed system.

In traditional optical imaging systems, multiple cameras or lenslet array should be used to image the partially occluded object. Comparing the method proposed in this article with traditional methods, in terms of the system, the method proposed in this article only requires a photodiode and optical fiber probe to achieve the same functionality at the detection end, with simpler hardware and without the need for image matching in stereo vision with multiple cameras, making subsequent image processing simpler. In terms of algorithms, we know that neural networks have enormous potential in image processing. However, a large amount of data is inevitably needed to train the network, and the databases needed for different scenarios are also different. The obstacle area segmentation algorithm adopted in this article does not distinguish between scenarios,

the algorithm is simple, does not require a large amount of pre-processing data, and has a wider applicability.

At the same time, the imaging system proposed in this article is highly flexible and can be combined with neural network algorithms and stereo vision. As we know, neural network algorithm is a commonly used method to realize image segmentation in machine vision. In the proposed method, neural network algorithms also can be used to divide the occluded area and object area. At the same time, the proposed method also can be combined with stereo vision technology to recover the occluded 3D object based on SPI. These works are what we’re going to do in the future.

#### REFERENCES

- [1] H. Zhang et al., “Super-resolution imaging of fluorescent dipoles via polarized structured illumination microscopy,” *Nature Commun.*, vol. 10, no. 1, pp. 1–10, 2019, doi: [10.1038/s41467-019-12681-w](https://doi.org/10.1038/s41467-019-12681-w).
- [2] W. Yu, X. Liu, X. Yao, C. Wang, G. Zhai, and Q. Zhao, “Single-photon compressive imaging with some performance benefits over raster scanning,” *Phys. Lett. A*, vol. 378, pp. 3406–3411, 2014, doi: [10.1016/j.physleta.2014.09.034](https://doi.org/10.1016/j.physleta.2014.09.034).
- [3] A. Velten, T. Willwacher, O. Gupta, A. Veeraraghavan, M. G. Bawendi, and R. Raskar, “Recovering three-dimensional shape around a corner using ultrafast time-of-flight imaging,” *Nature Commun.*, vol. 3, 2012, Art. no. 745, doi: [10.1038/ncomms1747](https://doi.org/10.1038/ncomms1747).
- [4] M. F. Duarte et al., “Single-pixel imaging via compressive sampling,” *IEEE Signal Process. Mag.*, vol. 25, no. 2, pp. 83–91, Mar. 2008, doi: [10.1109/MSP.2007.914730](https://doi.org/10.1109/MSP.2007.914730).
- [5] L. Olivieri et al., “Hyperspectral terahertz microscopy via nonlinear ghost imaging,” *Optica*, vol. 7, no. 2, pp. 186–191, 2020, doi: [10.1364/OPTICA.381035](https://doi.org/10.1364/OPTICA.381035).
- [6] H. Yu et al., “Fourier-transform ghost imaging with hard X rays,” *Phys. Rev. Lett.*, vol. 117, no. 11, 2016, Art. no. 113901, doi: [10.1103/PhysRevLett.117.113901](https://doi.org/10.1103/PhysRevLett.117.113901).
- [7] D. Pelliccia, A. Rack, M. Scheel, V. Cantelli, and D. M. Paganin, “Experimental X-ray ghost imaging,” *Phys. Rev. Lett.*, vol. 117, no. 11, 2016, Art. no. 113902, doi: [10.1103/PhysRevLett.117.113902](https://doi.org/10.1103/PhysRevLett.117.113902).
- [8] J. Teng, Q. Guo, M. Chen, S. Yang, and H. Chen, “Time-encoded single-pixel 3D imaging,” *APL Photon.*, vol. 5, no. 2, 2020, Art. no. 020801, doi: [10.1063/1.5139924](https://doi.org/10.1063/1.5139924).
- [9] Y. Qian, R. He, Q. Chen, G. Gu, F. Shi, and W. Zhang, “Adaptive compressed 3D ghost imaging based on the variation of surface normals,” *Opt. Exp.*, vol. 27, no. 20, pp. 27862–27872, 2019, doi: [10.1364/OE.27.027862](https://doi.org/10.1364/OE.27.027862).
- [10] D. Shi et al., “Adaptive optical ghost imaging through atmospheric turbulence,” *Opt. Exp.*, vol. 20, no. 27, pp. 27992–27998, 2012, doi: [10.1364/OE.20.027992](https://doi.org/10.1364/OE.20.027992).
- [11] J. Cheng, “Ghost imaging through turbulent atmosphere,” *Opt. Exp.*, vol. 17, no. 10, pp. 7916–7921, 2009, doi: [10.1364/OE.17.007916](https://doi.org/10.1364/OE.17.007916).
- [12] F. Li, M. Zhao, Z. Tian, F. Willomitzer, and O. Cossairt, “Compressive ghost imaging through scattering media with deep learning,” *Opt. Exp.*, vol. 28, no. 12, pp. 17395–17408, 2020, doi: [10.1364/OE.394639](https://doi.org/10.1364/OE.394639).
- [13] L. H. Zhang, Z. X. Bian, H. L. Ye, Z. R. Wang, K. M. Wang, and D. W. Zhang, “Restoration of single pixel imaging in atmospheric turbulence by Fourier filter and CGAN,” *Appl. Phys. B*, vol. 127, 2021, Art. no. 45, doi: [10.1007/s00340-021-07596-8](https://doi.org/10.1007/s00340-021-07596-8).
- [14] M. J. Sun et al., “Single-pixel three-dimensional imaging with time-based depth resolution,” *Nature Commun.*, vol. 7, 2016, Art. no. 12010, doi: [10.1038/ncomms12010](https://doi.org/10.1038/ncomms12010).
- [15] C. Gao, X. Wang, L. Gou, Y. Feng, and H. Cai, “Ghost imaging for an occluded object,” *Laser Phys. Lett.*, vol. 16, 2019, Art. no. 065202, doi: [10.1088/1612-202X/ab0c8d](https://doi.org/10.1088/1612-202X/ab0c8d).
- [16] B. Javidi, R. Ponce-Díaz, and S. - H. Hong, “Three-dimensional recognition of occluded objects by using computational integral imaging,” *Opt. Lett.*, vol. 31, no. 8, pp. 1106–1108, 2006, doi: [10.1364/OL.31.001106](https://doi.org/10.1364/OL.31.001106).
- [17] S. H. Hong and B. Javidi, “Distortion-tolerant 3D recognition of occluded objects using computational integral imaging,” *Opt. Exp.*, vol. 14, no. 25, pp. 12085–12095, 2006, doi: [10.1364/OE.14.012085](https://doi.org/10.1364/OE.14.012085).

- [18] D. H. Shin, B. G. Lee, and J. J. Lee, "Occlusion removal method of partially occluded 3D object using sub-image block matching in computational integral imaging," *Opt. Exp.*, vol. 16, no. 21, pp. 16294–16304, 2008, doi: [10.1364/OE.16.016294](https://doi.org/10.1364/OE.16.016294).
- [19] D. H. Shin, H. Yoo, C. W. Tan, B. G. Lee, and J. J. Lee, "Occlusion removal technique for improved recognition of partially occluded 3D objects in computational integral imaging," *Opt. Commun.*, vol. 281, pp. 4589–4597, 2008, doi: [10.1016/j.optcom.2008.06.026](https://doi.org/10.1016/j.optcom.2008.06.026).
- [20] J. J. Lee, B. G. Lee, and H. Yoo, "Image quality enhancement of computational integral imaging reconstruction for partially occluded objects using binary weighting mask on occlusion areas," *Appl. Opt.*, vol. 50, no. 13, pp. 1889–1893, 2011, doi: [10.1364/AO.50.001889](https://doi.org/10.1364/AO.50.001889).
- [21] Y. Rivenson, A. Rot, S. Balber, A. Stern, and J. Rosen, "Recovery of partially occluded objects by applying compressive Fresnel holography," *Opt. Lett.*, vol. 37, no. 10, pp. 1757–1759, 2012, doi: [10.1364/OL.37.001757](https://doi.org/10.1364/OL.37.001757).
- [22] R. Usami, T. Nobukawa, M. Miura, N. Ishii, E. Watanabe, and T. Muroi, "Dense parallax image acquisition method using single-pixel imaging for integral photography," *Opt. Lett.*, vol. 45, no. 1, pp. 25–28, 2020, doi: [10.1364/OL.45.000025](https://doi.org/10.1364/OL.45.000025).
- [23] C. Li, W. Yin, H. Jiang, and Y. Zhang, "An efficient augmented Lagrangian method with applications to total variation minimization," *Comput. Optim. Appl.*, vol. 56, no. 3, pp. 507–530, 2013, doi: [10.1007/s10589-013-9576-1](https://doi.org/10.1007/s10589-013-9576-1).
- [24] O. Sefi, Y. Klein, E. Strizhevsky, I. P. Dolbnya, and S. Shwartz, "X-ray imaging of fast dynamics with single-pixel detector," *Opt. Exp.*, vol. 28, no. 17, pp. 24568–24576, 2020, doi: [10.1364/OE.396497](https://doi.org/10.1364/OE.396497).